Surface analyses of low carbon steel and stainless steel in geothermal synthetic Na-Ca-Cl brine saturated with CO2

Marie Poulain, Jean-Charles Dupin, Kessein Eric Tillous, Jean-Bernard Ledeuil, Jean-Paul Serin, Pierre Cézac, Hervé Martinez

Results in Surfaces and Interfaces 7 (2022) 100040

Contents lists available at ScienceDirect

Results in Surfaces and Interfaces

journal homepage: www.elsevier.com/locate/rsurfi

Surface analyses of low carbon steel and stainless steel in geothermal synthetic Na-Ca-Cl brine saturated with CO_2

Marie Poulain [a,b], Jean-Charles Dupin [b], Kessein Eric Tillous [c], Jean-Bernard Ledeuil [b], Jean-Paul Serin [a], Pierre Cézac [a], Hervé Martinez [b,*]

[a] Universite de Pau et des Pays de l'Adour, E2S UPPA, LaTEP, Pau, France
[b] Universite de Pau et des Pays de l'Adour, E2S UPPA, CNRS, IPREM, Pau, France
[c] LabTech, Université Félix Houphouët-Boigny de Cocody, UFR SSMT, 22 B.P. 479, Abidjan, Cote d'Ivoire

ARTICLE INFO

Keywords:
Brine
Material corrosion
Geothermal corrosion pilot
Surface characterization

ABSTRACT

In a geothermal power plant, certain precautions should be taken to ensure a good efficiency. Indeed, it is important to avoid degassing of the geothermal fluid and to prevent corrosion issues. To address these problems, the gas–liquid equilibrium has to be controlled and the characteristics (composition, temperature…) of the fluid known as well as the nature of the material used.

For this reason, in this paper, a laboratory-scale device was developed in order to simulate natural like conditions and achieve corrosion tests. The corrosion behaviour of two materials, a carbon steel (DC01) and a stainless steel (304 L), has been investigated. The testing materials have been exposed to a synthetic brine which composition is similar to the Upper Rhine Graben water formation. The brine was saturated with 2 MPa of CO_2 and heated up to 50 °C and 100 °C.

Surfaces of tested metals were analysed by spectroscopic (XPS) and microscopic (SEM) methods in order to characterize corrosion products and to get more information onto the corrosion mechanisms process.

The use of the laboratory prototype coupled with surface analysis methods allowed to better understand CO_2 corrosion in geothermal environment. The role of the brine chemistry and the impact of temperature and CO_2 dissolved concentration have been studied in this work. Indeed, different natures of corrosion products regarding the material composition and microstructure have been highlighted. A mixture of $CaCO_3$ and $FeCO_3$ scale is identified on the carbon steel whereas the stainless steel exhibits a mixture of $Cr(OH)_3$ and $FeCO_3$ on its surface.

1. Introduction

The development of renewable energies is obviously necessary to ensure the energy transition. Deep geothermal energy is receiving growing attention because of numerous advantages: production of heat and electricity, local energy, independent of climatic conditions and generally low CO_2 emissions (Agemar et al., 2014). In a geothermal power plant, some components such as heat exchangers are essential. To maintain a good efficiency in heat exchanger, gas presence must be avoided into it. Hence, degassing phenomenon must be prevented during the geothermal fluid rise in the well by anticipating the bubble pressure. Moreover, another key point to ensure an optimal use of heat exchanger is to inhibit corrosion (Corsi, 1986). The knowledge of the fluid is essential first to thermodynamically characterize liquid–vapour equilibrium to avoid degassing and then to prevent corrosion since it may contain species responsible for corrosion: chlorides, sulphates, dissolved carbon dioxide. Kaya and Hoshan (2005), Iberl et al. (2015), Nogara and Zarrouk (2018a)… Furthermore, temperature and pressure must be considered as their variation could impact corrosion process by the deposit of corrosion products (Dugstad, 1998; Palacios and Shadley, 1991). Steel composition and microstructure must be also regarded, as they involve some specificities in the final corrosion products layer (Iberl et al., 2015; Nogara and Zarrouk, 2018b).

To handle these problems, an accurate knowledge of the nature of the geothermal fluid (salt composition, gas phase, pH…) is required since it is dependent on the location where it is collected. In France, deep geothermal energy has mainly been developed in the Upper Rhine Graben. Fluids encountered in this area are classified as highly salted with a Total Dissolved Species (TDS) close to 90 g L^{-1} (Sanjuan et al., 2016). This brine contains dissolved gas, mainly CO_2, which participate in the acidification of the fluid.

Many corrosion studies in geothermal environment have been carried out (Corsi, 1986; Kaya and Hoshan, 2005; Carter and Cramer, 1992; Culivicchi et al., 1983; Faes et al., 2019; Frick et al., 2011;

* Correspondence to: IPREM CNRS UMR5254 – Helioparc – 2, Avenue du Président Pierre Angot 64053 Pau Cedex 9, France.
E-mail address: herve.martinez@univ-pau.fr (H. Martinez).

https://doi.org/10.1016/j.rsurfi.2022.100040
Received 27 July 2021; Received in revised form 20 December 2021; Accepted 10 January 2022

Table 1
Chemical composition (wt.%) of tested metals obtained by Spark Optical Emission Spectrometry (Spark OES).

Sample	C	Si	Mn	P	S	Cr	Mo	Ni	Cu	Ti	Fe
DC01	0.039	0.022	0.210	0.0078	0.0028	0.0127	0.0017	0.0035	0.0110	0.0020	99.6
304L	0.021	0.047	1.492	0.025	<0.0005	17.6	0.24	8.81	0.48	0.0028	70.1

Keserović, 2014). Nevertheless, studies on material corrosion in the Upper Rhine Graben fluid remain scarcer (Mundhenk et al., 2013a,b, 2014; Huttenloch et al., 2019). In alkaline conditions, an increase in temperature generally involves a corrosion rate enhancement (Prawoto et al., 2009). Nevertheless, in the CO_2 media, the corrosion behaviour is more complicated. Indeed, the precipitation of iron carbonate on the carbon steel surface can slow down the corrosion process. Many parameters such as pH or temperature can affect the formation of the $FeCO_3$ scale and its properties. As an example, Dugstad has studied the film formation on a carbon steel during CO_2 corrosion at several temperatures (Dugstad, 1998). Indeed, the film formed at high temperature ($T > 60$ °C) is dense and more protective than the film formed at low temperature ($T < 40$ °C) which is porous and less adherent.

More recently, a study has been conducted on the kinetics aspects of high temperature CO_2 corrosion of a carbon steel in geothermal NaCl-fluids and associated film formation (Mundhenk et al., 2020). However, this study has been carried out in synthetic geothermal water only containing NaCl salt and it is known that water chemistry can also affect the formation of $FeCO_3$ scale.

Esmaeely et al. have studied the impact of the calcium cations Ca^{2+} on the CO_2 corrosion of a carbon steel sample immersed into a 1 wt.% NaCl solution at 80 °C (Esmaeely et al., 2017). When calcium ions concentration was low (<100 ppm) a $FeCO_3$ protective film was formed on the surface steel. At higher Ca^{2+} concentrations the precipitation of a non-protective film of $CaCO_3$ predominated. Nevertheless, this study was conducted at low CO_2 partial pressure ($p_{CO_2} = 0.05$ MPa).

Stainless steels usually contain alloy element which participate in reducing the corrosion rate, especially a high chromium content (>10.5 wt%) (Nogara and Zarrouk, 2018b). Substrate surface composition is then highly important in the result of the corrosion event. The evaluation of the corrosion resistance of high-alloyed materials in the North German Graben was previously studied by Klapper et al. (2012). Electrochemical and exposure tests were conducted on several specimens, included austenitic stainless steel, and the results shown that these materials exhibit a susceptibility to corrosion pitting especially at high temperature. These results are in concordance with those observed in other studies (Yevtushenko et al., 2010; Yevtushenko and Baessler, 2012), with a rapid initiation of pitting in high chloride brines saturated with CO_2. Indeed, few investigations conducted on CO_2 corrosion in brines have shown that the stainless steel surface is generally covered up with a protective chromium oxide layer (Guo et al., 2012; Xu et al., 2013; Liu et al., 2016). A recent work has studied the thermodynamic and kinetic formation of corrosion scale on the stainless steel surfaces in geothermal environment at 200 °C. This paper revealed the presence of $FeCr_2O_4$, $Cr(OH)_3$ and $FeCO_3$ scales depending on the CO_2 partial pressure of the experiments (Yue, 2020).

To complete a corrosion study, most of the time, weight loss measurements and electrochemical analyses are used to determine the corrosion rate (Mundhenk et al., 2013a,b, 2014; Huttenloch et al., 2019). These data are important in the choice of the material used for tubing and/or casing structures. Moreover, coupled surface analyses by X-ray Photoelectron Spectroscopy (XPS) and Scanning Electron Microscopy (SEM) surface analyses could even be useful to precise the corrosion phenomenon as it is a surface event and to chemically identify the corrosion products. One of the few research works, from Heuer and Stubbins has shown the concomitant formation of $FeCO_3$ and iron oxide films from 40 °C on the mild steel surface by XPS (Heuer and Stubbins, 1999). Lopez et al. have correlated a possible influence of the microstructure with the corrosion product formation with XPS and SEM methods (Lopez et al., 2003). Two different steels were dipped into a NaCl brine at 40 °C. Both steels surfaces were covered up with a scale consisting of the same chemical components (a mixture of $FeCO_3$ and Fe_3C) but with different compositions. For Cr-alloy, the work of Guo et al. using XPS characterization, has permit to identify a $Cr(OH)_3$ phase as the main corrosion product when the metal is immersed into a CO_2-saturated geothermal fluid (Guo et al., 2016).

Although the impact of temperature and microstructure is clearly identified in the geothermal corrosion, the present work reports the behaviour of a carbon steel and stainless steel under high CO_2 pressure, in more real environmental conditions and focus on their surface characterization. In this study, a laboratory geothermal corrosion prototype device was developed to run investigations at high CO_2 pressures and high temperatures. This first work was achieved with DC01 carbon steel and 304L stainless steel substrates exposed to a synthetic brine with a composition similar to the Upper Rhine Graben geothermal fluid: a mixture of NaCl and $CaCl_2$ saturated with CO_2. The corrosion studies have been carried out at 50 °C and 100 °C at 2 MPa to reproduce the conditions encountered in a heat exchanger (Mouchot et al., 2018). In this study, the corrosion characterization was carried out on materials surfaces using the complementarity of XPS and SEM methods. Some systematic analyses were conducted to determine the surface chemistry of the metal substrate after 1 h, 48 h and 500 h of brine exposure. The ultimate goal is to propose a relevant process of surface reactivity according to the composition of the brine and the experimental conditions (temperature, pressure and time of exposure).

2. Materials and methods

2.1. Metals

Two metals provided by Neyco, a carbon steel DC01 and a stainless steel 304L, were immersed into CO_2-saturated geothermal brine. Their chemical composition obtained from optical emission spectra are given in Table 1. Beside iron and carbon (0.039 wt%), some additional elements are detected (such as manganese, aluminium and silicon) for DC01 mild steel. Concerning the stainless steel 304L, results indicate that the sample contains 70.1 wt% of iron, 17.6 wt% of chromium and finally 8.8 wt% of nickel.

Metals microstructures have been highlighted by optical microscopy after a metallographic preparation consisting first in polishing the surface up to 1 μm and then chemically attacking the sample with Nital©. Micrographs are presented in Fig. 1. The carbon steel exhibits a ferrite (F) dominated microstructure with some dark particles which could be attributed to carbide (C) phase. Moreover, linear structures into ferrite grain could represent the initiation of perlitic (P) growth which is limited for mild steel with a low carbon content (less than 0.05 wt.%). The stainless steel microstructure consists in austenite (A) grain. As for the carbon steel, the darker particles could be related to carbide phase.

Before exposure to the geothermal fluid, the steel coupons were cut as square samples (1 cm × 1 cm × 2 mm for DC01 carbon steel and 2 cm × 2 cm × 3 mm for 304L stainless steel). Herein, the dimensions of the specimens are given for guidance since this study is focused on surface characterization. However, this information must be carefully considered for corrosion rate calculation since the ratio of exposed surface area to volume of solution must be limited to not be less than 30 mL/cm^2. Nogara and Zarrouk (2018b) The samples were prepared according to the ASTM G1-03 (ASTM G1-03, 2018), Standard Practice for Preparing, Cleaning, and Evaluating Corrosion Test Specimens. Several protocols of specimen preparation, with different abrasive paper, have

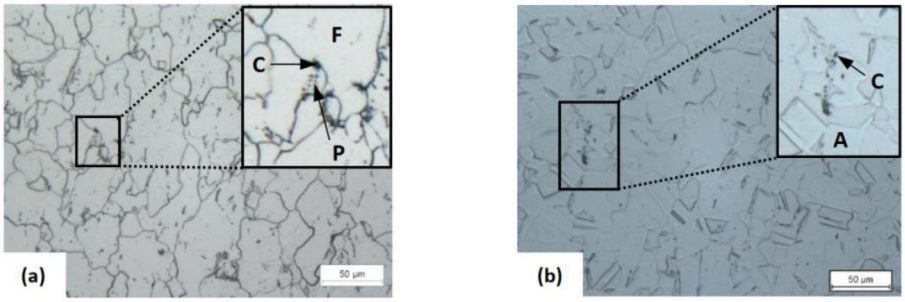

Fig. 1. Micrographs of (a) carbon steel DC01 microstructure and (b) stainless steel 304L microstructure.

been tested in a preliminary study. Then, systematic XPS analyses were done on the material surface to check the presence of the iron metal Fe^0. The most suitable preparation was found to be the successively polishing with SiC abrasive paper (500, 800 and 1000 grit), degreased with acetone, washed with water and dried 24 h in a desiccator. Nevertheless, a part of the native oxidation layer at the material surface remains after the sample preparation.

2.2. Geothermal fluid

The composition of the synthetic brine was based on the Upper Rhine Graben formation water (from Soultz-sous-Forêts, France) (Sanjuan et al., 2016). This brine is saturated with carbon dioxide. The pressure was fixed at 2 MPa which is closed to the conditions encountered in a heat exchanger. The thermodynamic characterization of this type of fluid have been carried out in our previous study (Poulain et al., 2019). Indeed, we measured the CO_2 solubility in two synthetic brines which composition were closed to the Upper Rhine Graben fluid: Na-Ca-Cl and Na-Ca-K-Cl brines between 1 and 20 MPa at 50, 100 and 150 °C The obtained results showed that the Upper Rhine Graben fluid could be approached by a mixture of NaCl at 1.2 mol kg^{-1} of water and $CaCl_2$ at 0.2 mol kg^{-1} of water. The Fig. 2 summarized the experimental values of solubility obtained for CO_2-NaCl-$CaCl_2$ system at 2 MPa and the corresponding CO_2 solubility curves calculated with PSUCO2 and PhreeqC. As a reminder, at 2 MPa, concentrations of carbon dioxide dissolved at 50 °C and 100 °C are respectively 0.257 and 0.142 mol kg^{-1} of water. Such data have significance for corrosion study since the CO_2 dissolved concentration could directly impact the formation of corrosion product and therefore increase or slow down the corrosion process. Despite the device is not including in-situ pH measurements, the pH of brines were calculated using PhreeqC geochemical model. The pH of the solution at 50 °C has been estimated to be around 3.2 whereas it was 3.4 at 100 °C

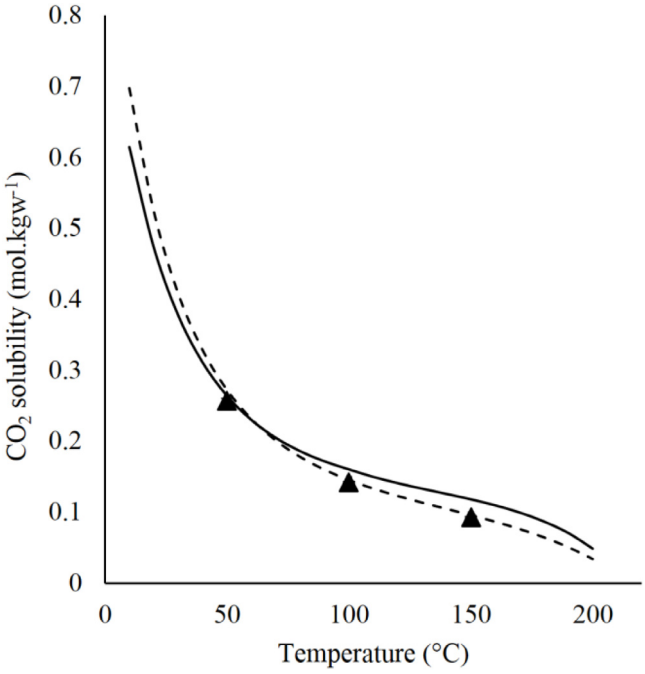

Fig. 2. CO_2 solubility in Na-Ca-Cl solution at 2 MPa : experimental data (▲), calculated with PSUCO2 (solid line) and calculated with PhreeqC (dashed line) from Poulain et al. (2019).

2.3. Geothermal corrosion prototype device

Because of the great importance of CO_2-brine equilibrium on the corrosion, a prototype device has been developed. A specific note has been drawn up for the design of a pilot able to operate in very high experimental conditions corresponding to deep geothermal constraints up to 200 °C and up to 20 MPa. This device, presented in Fig. 3, was built by Armines/CTP to conduct corrosion tests in specific geothermal brine saturated with CO_2. The device is very original with two ovens, containing each two titanium autoclaves (Fig. 4a). The main particularity of this device is the possibility to conduct several corrosion tests at the same time with independent conditions of temperature, brine chemistry or gas nature, thanks to the four autoclaves. A temperature probe (PT100 Ohms) is placed on the top and the bottom of each cell in order to control the temperature homogeneity. Each reactor is even connected to a pressure sensor (Keller PAA 35 XHTC).

Fig. 3. Geothermal corrosion prototype device.

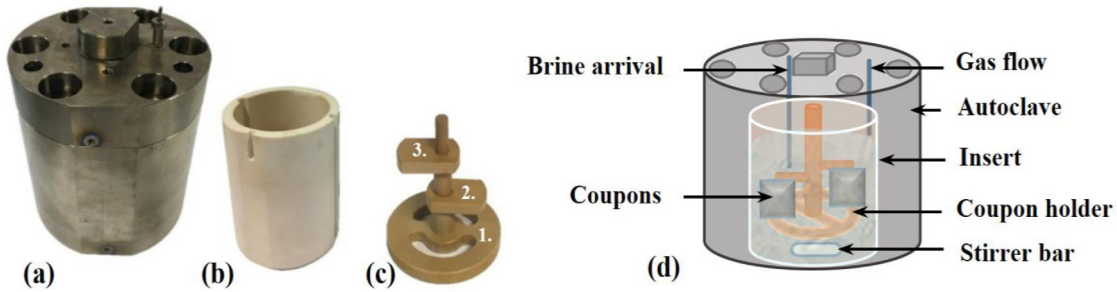

Fig. 4. Photographs of (a) the autoclave, (b) the insert and (c) the coupon holder with several coupons positions 1. in the aqueous phase; 2. at the gas/liquid interface; 3. in the gas phase, (d) Schematic representation of an autoclave.

A SITEC rupture disk, which burst pressure is set to 22.5 MPa, has been placed on each reactor to automatically stop the operating processes in case of cells overpressurization.

A metal substrates holder (Fig. 4c) made of PEEK, was designed to expose the samples either in the aqueous phase, in the gaseous phase or even at the interface gas/liquid according to three different height stages. Before the corrosion experiment, this sample holder is placed within an inert glass reinforced-PTFE insert (Fig. 4b) which avoids any contact and galvanic effect between the metal specimens and the autoclave. Aqueous phase coming in the insert is continuously stirred during experiments with a magnetic stirrer located at its bottom. A schematic representation of the coupons placement in the sample holder within the reactor is reported in Fig. 4d. The liquid and gas inlet are placed at the top of each reactor. Then, four identical autoclaves are then placed by pairs into the ovens.

2.4. Operating procedure

Specimens are placed into the reactor. After setting the vacuum within the different components of the device, approximately 40 cm^3 of synthetic brine gets into the autoclave. The solution is then deoxygenated by nitrogen bubbling during 30 min. The temperature is fixed to the expected value for the experiment. Then, carbon dioxide fills in the autoclave network and a heavy stirring of the brine is applied (800 rpm). Once the gas–liquid equilibrium is reached, the stirring speed is lowered down to 200 rpm for the time of the experiment. In this study, metal samples were exposed to a synthetic brine saturated with 2 MPa of CO_2 simultaneously heated up to 50 °C or 100 °C during 1 h, 48 h and 500 h. Finally, the metal specimens were released from the autoclave, rinsed with distilled water before being dried in a desiccator.

2.5. Corrosion characterization

In this study, the carbon steel surfaces were systematically analysed before and after exposure to the geothermal fluid by Scanning Electron Microscopy (SEM) and X-ray Photoelectron Spectroscopy (XPS). Concerning the stainless steel, sample size constraints have led to observe the sample surface by optical microscopy rather than by SEM before doing the XPS characterization.

SEM investigations were conducted with a JEOL JEAMP 9500F Auger Spectrometer (JEOL Ltd, Tokyo, Japan). This machine needs to work under UHV conditions ($P < 2.10^{-7}$ Pa). SEM images were acquired using an acceleration voltage of 15 kV and a low current of 1 nA. They have been recorded at several magnifications to get more information.

Optical microscopy images were recorded with an optical microscope Axiolab 5 (Zeiss). Here again, different magnifications have been used to take microscopic images.

Surface analyses by XPS were carried out with a Thermo K-alpha spectrometer (ThermoFisher Scientific) operating under ultra-vacuum (10^{-9} mbar). This device used the monochromatized Al-Kα radiation (1486.6 eV) as X-ray source. An argon dry glove box is directly connected to the machine. The radiation is microfocused on the surface sample (ellipsoidal spot of 400 μm diameter). A charge compensation system based on low energy electrons was used. First, survey spectra were recorded from 0 to 1350 eV with a pass energy (PE) of 200 eV. Then core ionization spectra were recorded with a higher resolution at PE of 40 eV. All spectra were fitted with CasaXPS© software. Binding energy of the C 1s peak due to the presence of adventitious carbon has been set up to 285 eV. Peak fitting is performed with a non-linear Shirley type background. GL(30) corresponding to a combination of Gaussian (70 %) and Lorentzian (30 %) functions were used to fit experimental curves for most of the components except for iron, chromium and nickel spectra. Indeed, asymmetry observed involves to use LA(α, β, m) line shapes for metallic core lines, where α and β represent the spread of either side of the tail of the Lorentzian component. The coefficient have been previously determined by Biesinger et al. LA(1.2, 4.8, 3) is used for Fe^0, LA(1.4, 4, 5) for Cr^0 and LA(1.1, 2.2, 10) for Ni^0 (Biesinger et al., 2011). Moreover, the components associated to iron oxide and chromium oxide environment have been fitted using a A(α, β, n)GL(m) line shape with is a Gaussian–Lorentzian function modified by an asymmetry. The coefficient used in this study were A(0.15, 0.65, 0)GL(0) for iron oxide and A(0.10, 0.65, 0)GL(0) for chromium oxide. All experimental XPS spectra are plotted by dotted line whereas the different components and resulting spectra are represented by solid lines. Quantitative analyses were performed using Scofield's Relative Sensitivity Factors (RSF).

3. Results and discussion

3.1. Carbon steel

Carbon steel was the first specimen studied as most of the geothermal structures all around the world still include it for specific parts of the geothermal power plant exchangers or even for casing tubes. Once withdrawn out of the corrosion chamber, after the first hour of exposure at 50 °C, the sample surface changed with shiny appearance loss (Fig. 5). 48 h immersion in the geothermal fluid gets the surface darker and finally, a yellow–orange deposit is perceptible on a portion of the sample surface with a 500 h exposure into the brine. In this case, some pits of corrosion are randomly spread over the yellow–orange area. Dipped into the brine heated up to 100 °C, the sample is affected and the visual analysis of the surface reveals a change but the evolution is less pronounced with exposure time. Nevertheless, surface colour change attest of some chemical reactions occurring during the sample immersion into the geothermal fluid.

In order to understand events taking place onto the carbon steel surface during immersion into the CO_2 saturated geothermal fluid, SEM images were recorded at different magnification modes (Fig. 6).

After 1 h of immersion into the fluid at 50 °C, the SEM image reflects that the metal has been dissolved (Fig. 6a). Moreover, at lower magnification (not shown in the paper), polishing scratches were still

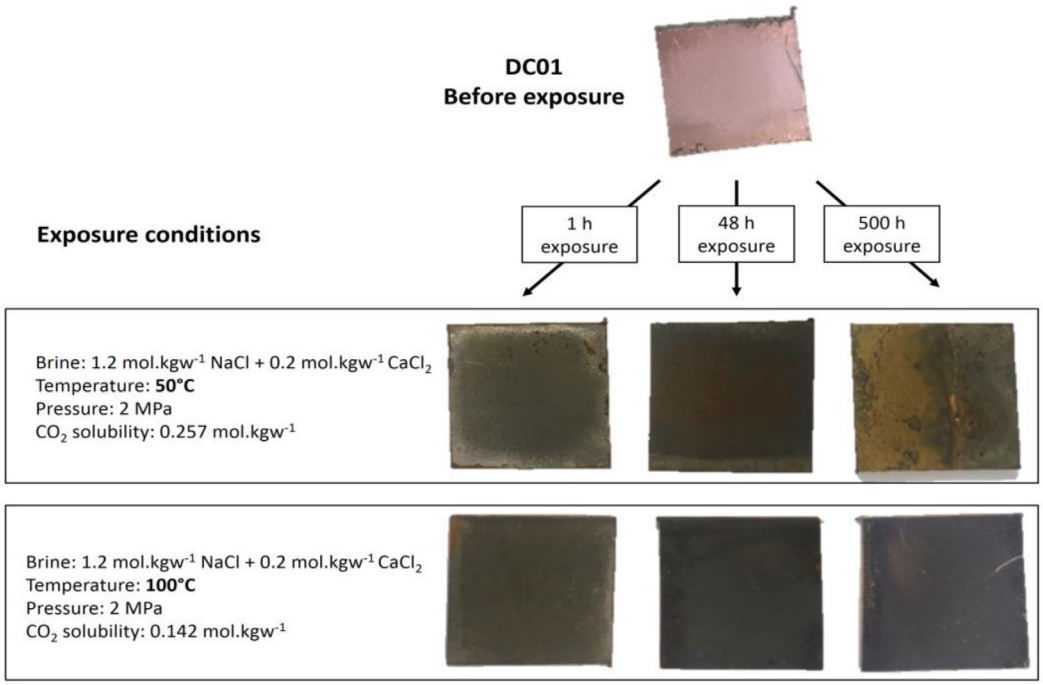

Fig. 5. Photographs of the carbon steel DC01 specimens before and after their immersion into the geothermal fluid saturated with 2 MPa of CO_2 at 50 °C and 100 °C during 1, 48 and 500 h. (For interpretation of the references to colour in this figure legend, the reader is referred to the web version of this article.)

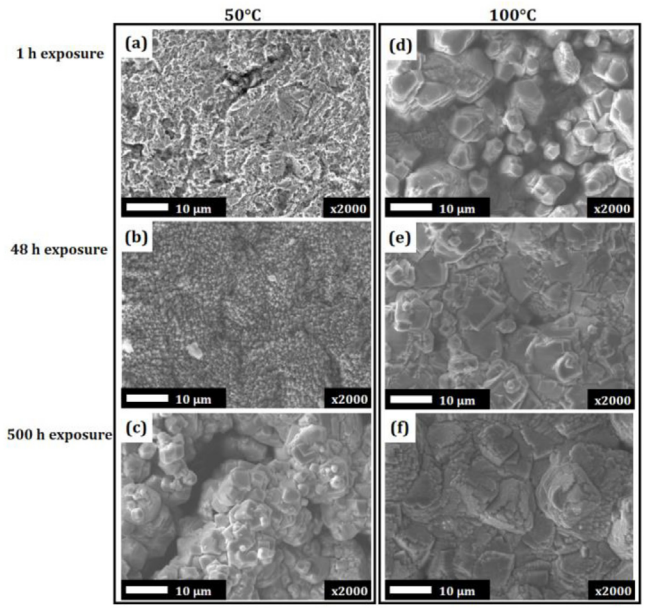

Fig. 6. SEM images of the carbon steel DC01 specimens after immersion into the geothermal fluid saturated with 2 MPa of CO_2 at 50 °C during 1 h (a); 48 hours (b); 500 hours (c) and at 100 °C during 1 h (d); 48 h (e) and 500 h (f).

visible. For longer exposure time, a corrosion product deposit appears. The nucleation of crystallites is clearly visible after 48 h immersion (Fig. 6b) and their size increases significantly with the immersion time (Fig. 6c). Similar observations were made by Tavares et al. (2015).

On SEM images for 100 °C brine conditions, a corrosion product layer appears on the carbon steel surface from the very first immersion hour (Fig. 6d). As previously observed at 50 °C, crystallites size grows up when increasing the exposure time (Fig. 6e and 6f) but at 100 °C the development speed seems higher and the layer formed is more compact and denser. A densification of the corrosion product with the temperature increase has been demonstrated by Nazari et al. (2010). The different crystallites morphologies would mean the corrosion product layer is probably composed of different phases. To know more about the chemical nature of the layer and relative content onto the extreme surface, some XPS analyses were carried out for the different sets of immersion hours — temperature.

Before brine exposure, the C 1s spectrum (Fig. 7) of the carbon steel surface (XPS enables a 10 nm depth analysis) is composed of four components corresponding to C–C/C–H, C–O, O–C=O and some carbide environments in very small content (Fig. 7a). The presence of a carbide assigned peak, located at 282.9 eV as reported elsewhere (Wang et al., 2012), is probably due to the SiC grains inclusion from the polishing paper used during the surface preparation step.

After one hour exposure at 50 °C (Fig. 7b), the proportion of the carbide peak has been divided by two (Table 2) probably due to the beginning of the carbon steel oxidization and the growth of a covering layer. After 48 h of immersion, the carbide component disappears whereas a new component is detected at 289.7 eV (Fig. 7c) attributed to carbonates (Heuer and Stubbins, 1999; Cui et al., 2006; Wu et al., 2004). When the immersion lasts 500 h (Fig. 7d), this component significantly enhances (from 2.9 to 15.4 at.%) and slightly shifts up to 289.9 eV, attesting of a modification of the carbonates local environment.

For higher temperature of the geothermal fluid (100 °C), the C 1s spectrum, after the first hour of immersion, drastically changes. Indeed, on the one hand the carbide component situated at 282.9 eV is no longer detected unlike to the three components C–C/C–H, C–O, O–C=O still clearly visible (Fig. 7e). On the other hand, an intense component associated with carbonates is located at 289.9 eV. Scales of carbonates are observed on the carbon steel surface from the first hour of exposure at 100 °C. When the coupon is immersed during 48 h, the proportion of the carbonates rises up from 11.6 to 16 at.% (Fig. 7f). For longer immersion time, this contribution diminished down to 14 at.% as shown in Fig. 7 g and Table 2.

The Fe $2p_{3/2}$ spectrum before immersion shows a small component at 706.7 eV (Fig. 8a), attributed to the presence of iron metal Fe^0. The experimental profile is also fitted into two others components situated

Table 2
Binding energies (BE) and atomic percentages (at.%) of the chemical environment identified by XPS on the carbon steel DC01 surface before and after exposure to the geothermal fluid at 50 and 100 °C during several exposure times.

	Before exposure			50 °C					100 °C				
						1 h exposure	48 h exposure	500 h exposure			1 h exposure	48 h exposure	500 h exposure
Orbital	BE (eV)	Assignment	at.%	BE (eV)	Assignment	at.%	at.%	at.%	BE (eV)	Assignment	at.%	at.%	at.%
C 1s	282.9	Carbide	2.0	282.9	Carbide	1.1			285	C–C/C–H	7.3	9.6	11.7
	285	C–C/C–H	23.7	285	C–C/C–H	20.3	5.9	6.1	286.5	C–O	1.1	2.1	1.6
	286.5	C–O	9.0	286.5	C–O	4.1	2.6	1.1	288.6	O–C=O	0.7	1.0	1.3
	288.6	O–C=O	4.4	288.6	O–C=O	2.6	0.8	1.2	289.9	CO_3^{2-}	11.6	16.0	14.0
				289.7	CO_3^{2-}		2.9	15.4					
Ca 2p	347.5	$CaCO_3$	0.2	347.3	$CaCO_3$		1.7	1.4	347.3	$CaCO_3$	5.6	2.0	2.0
	351	$CaCO_3$	0.1	350.8	$CaCO_3$		0.9	0.7	350.8	$CaCO_3$	2.8	1.0	1.0
				355.4	$CaCO_3$ sat.		0.05	0.04	355.4	$CaCO_3$ sat.	0.2	0.1	0.1
				359	$CaCO_3$ sat.		0.05	0.03	359	$CaCO_3$ sat.	0.2	0.1	0.1
Cl 2p				198.5	NaCl	0.4	0.2	0.5	198.5	NaCl	0.2	0.1	0.1
				200	NaCl	0.2	0.1	0.2	200	NaCl	0.1	0.05	0.05
Fe 2p3/2	706.7	Fe^0	3.3	706.7	Fe^0	1.1			710.3	$FeCO_3$	1.2	7.2	6.2
	708.9	Fe^{2+}	1.2	709	Fe^{2+}	0.5			711.2	Fe^{3+}	6.4	1.6	1.6
	710.8	Fe^{3+}	6.5	710.3	$FeCO_3$			7.5	715	$FeCO_3$ sat.	0.4	2.5	1.6
	714.5	Fe^{2+} sat.	0.3	711.2	Fe^{3+}	9.5	12.2	2.1	719.2	Fe^{3+} sat.	0.3	0.1	0.1
	718.8	Fe^{3+} sat.	0.2	714.5	Fe^{2+} sat.	0.1							
				715	$FeCO_3$ sat.			2.4					
				719.2	Fe^{3+} sat.	0.2	0.6	0.1					
Mn 2p	641.6	MnO	0.2	641.6	MnO	0.8	0.2		641.6	MnO	0.2		
N 1s	400	NH_3	0.7	400	NH_3	0.8			400	NH_3			
Na 1s				1072	NaCl		0.7	0.6	1072	NaCl		0.3	0.2
O 1s	530	Oxide	22.8	530	Oxide	25.8	27.4	5.2	530	Oxide	14.2	3.3	6.0
	531	Hydroxide	5.1	531	Hydroxide	17.2	28.3	5.6	531	Hydroxide	6.3	2.1	6.2
	531.5	O–C=O	10.2	531.5	O–C=O	9.5	1.5	2.1	531.5	O–C=O	1.4	1.5	2.7
	533	C–O	6.7	531 .9	CO_3^{2-}		9.4	43.6	531 .9	CO_3^{2-}	36.6	44.3	38.2
				533	C–O	1.9	1.1	1.7	533	C–O	1.2	2.6	1.7
Si 2p	100.5	Si–C	2.3	99.5	Si–Si	0.2	2.0	1.7	99.5	Si–Si	1.2	2.0	1.3
	102	Si–CO, SiOx...	1.1	100.5	Si–C	2.6			102	Si–CO, SiOx...	0.8	0.7	2.4
				102	Si–CO, SiOx...	1.1	1.4	0.8					

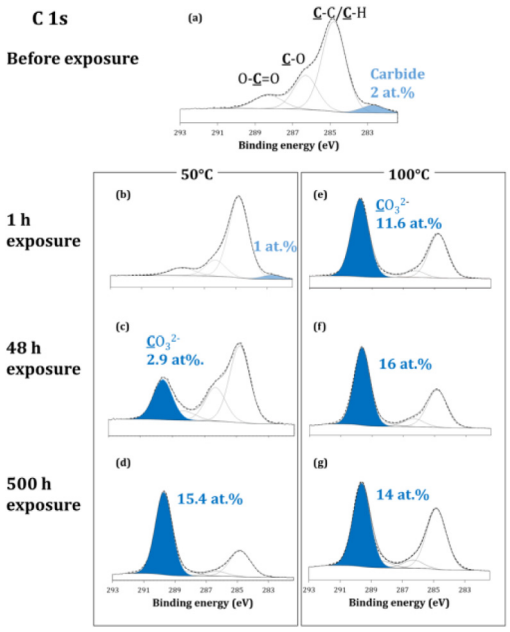

Fig. 7. C 1s XPS spectra of the carbon steel DC01 specimens before immersion (a) and after immersion into the geothermal fluid saturated with 2 MPa of CO_2 at 50 °C during 1 h (b); 48 h (c); 500 h (d) and at 100 °C during 1 h (e); 48 h (f) and 500 h (g).

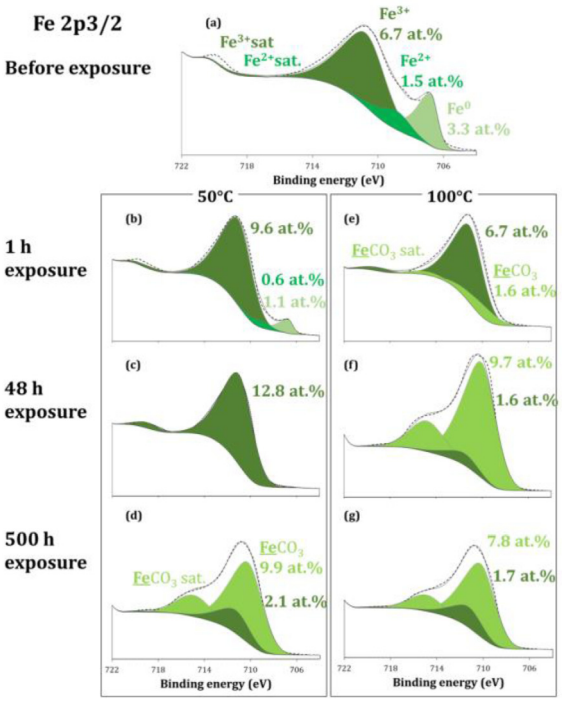

Fig. 8. Fe 2p3/2 XPS spectra of the carbon steel DC01 specimens before immersion (a) and after immersion into the geothermal fluid saturated with 2 MPa of CO_2 at 50 °C during 1 h (b); 48 h (c); 500 h (d) and at 100 °C during 1 h (e); 48 h (f) and 500 h (g).

at 708.9 eV and 710.8 eV corresponding respectively to the Fe^{2+} and Fe^{3+} environments. Some satellite peaks of the former components are found at 714.5 eV and 718.8 eV confirming the iron oxidation states (Biesinger et al., 2011). After 1 h of brine exposure at 50 °C, the iron metal component is less intense (3.3 to 1.1 at.%) as well as the reduction of the proportion of the Fe^{2+} components, as shown in Fig. 8b and Table 2. Furthermore, the Fe^{3+} components get higher. These evolution of composition suggest the corrosion process begun with the formation of oxide scales. The formation of this oxide layer could be explained by the remaining presence of oxygen before deoxygenating the solution by nitrogen bubbling. Indeed, specimens were exposed to a solution which could contains oxygen during 30 min and then were tested during 1 h at experimental conditions without oxygen. At short time of exposure, it is assumed that an oxidation of Fe^{2+} in Fe^{3+} in the presence of remaining oxygen has occurred, resulting in the formation of this oxide layer. From 48 h of steel immersion into the geothermal brine at 50 °C, the Fe^0 and Fe^{2+} components are no longer identified on

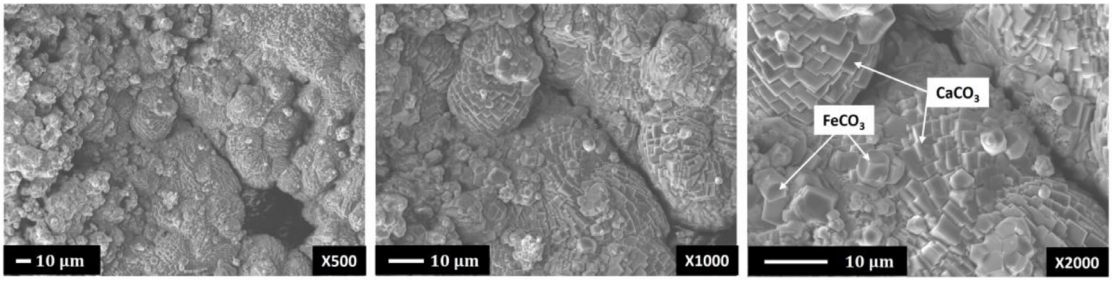

Fig. 9. SEM images of crystals distribution on the surface of the carbon steel exposed to the brine at 50 °C during 500 h.

Fe 2p the spectrum (Fig. 8c); the layer is probably thicker than 10 nm, and the XPS method can then only reach and specify the chemistry at the extreme surface. In addition, the absence of any Fe 2p peak in the energetic region of iron carbonates (around 710.3 ± 0.2 eV/main component and 715 ± 0.2 eV/satellite (Heuer and Stubbins, 1999; Cui et al., 2006; Wu et al., 2004)) is confirmed. Thus, the carbonates scales identified from the analysis of the C 1s spectrum of the carbon steel exposed at 50 °C during 48 h are not made of iron carbonates deposit. However, considering the analysis of the calcium Ca 2p spectrum (not shown in the paper) and the quantitative analysis presented in Table 2, carbonates ions could coordinate with calcium to form $CaCO_3$ on the surface.

After 500 h of immersion into the brine at 50 °C, the chemical analysis of the Fe $2p_{3/2}$ spectrum shows iron oxide is still detected (Fig. 8d). Nevertheless, the most remarkable change is the appearance of an intense component (7.5 at.%) and an associated satellite (2.4 at.%) assigned to an iron carbonates environment (Fig. 8d). As a reminder, in these conditions of temperature and exposure time, the quantitative analysis showed that the proportion of carbonates in the C 1s spectrum was around 15.4 at.%, content high enough to consider the iron carbonates are not the only carbonates corrosion products on the surface. Then, considering both Fe, Ca and C quantities at 50 °C, the carbon steel exposed during 500 h would be covered up with a mixture of siderite $FeCO_3$ and calcite $CaCO_3$. This result corroborates the slight C 1s BE positive shift of 0.2 eV of the carbonate component. In fact, the electronegativity of iron is greater than for calcium one. Thus, the C 1s carbonates peak would be located at higher binding energy when the major corrosion product is siderite.

SEM images (Fig. 9) of this sample display rhombohedral crystals of $CaCO_3$ and hexagonal crystals $FeCO_3$ on the carbon steel surface, confirming that the corrosion film product consists in a mixture of siderite and calcite. Moreover, $FeCO_3$ crystals seem to be placed above those of $CaCO_3$, allowing us to confirm that the growth of iron carbonate layer is posterior to that of calcium carbonate under these experimental conditions.

Finally, it is important to precise that surface analyses were made before photos (Fig. 5) and specimens were exposed to air after surface characterization. So, we assume that carbonate scale such as siderite could have oxidized resulting on the yellow–orange deposit observed on the photo of Fig. 5, which seems like rust. Heuer and Stubbins has pointed out such an iron carbonates scale formation on carbon steel could suddenly oxidize into Fe_2O_3 when exposed to air (Heuer and Stubbins, 1999).

The XPS analysis of the carbon steel exposed 1 h into the fluid at 100 °C shows the surface is mainly composed of iron oxide (Fig. 8e and Table 2). Iron carbonates are detected in small proportion (1.6 at.%) in accordance with the C 1s spectrum in the same experimental conditions. However, the quantitative results confirm the surface is even covered up with $CaCO_3$ scales. With a longer immersion time (48 h), the proportion of iron carbonates drastically increases (from 1.6 up to 9.7 at.%) and the corrosion product consists into a mixture of siderite and calcite with $FeCO_3$ as major component (Fig. 8f). After 500 h of immersion into the geothermal fluid, the carbon steel surface is always a mixture of $FeCO_3$ and $CaCO_3$ but the $FeCO_3$ phase is less prominent (Fig. 8 g) as ascertained by the decrease of C 1s carbonates component (BE = 289.9 eV). On the Fe 2p spectrum, iron oxide environment is now more easily detected probably meaning an oxide scale would overlay the carbonates scale. The previous work of Heuer and Stubbins is in agreement with this observation (Heuer and Stubbins, 1999).

In addition, the XPS analysis of other element such as manganese, one of the main alloying element in DC01 carbon steel (Table 1), has helped to confirm previous explanations. Before exposure, the carbon steel sample exhibits a small quantity (0.2 at.%, Table 2) of manganese oxide MnO, with a Mn2p $_{3/2}$ peak located at 641.6 eV (Biesinger et al., 2011). For brine temperature of 50 °C, an increase of MnO proportion is perceived after one hour of immersion, in relation with the beginning of carbon steel oxidation. Then, the MnO proportion at the surface diminishes for 48 h exposure and finally the oxide layer disappears when the coupon is immersed 500 h into the geothermal fluid. Indeed, the carbonates layer, the main corrosion product, spreads progressively over the whole specimen surface and gets thicker with immersion time. Under 100 °C conditions, manganese oxide at the carbon steel surface after 48 and 500 h, is no longer identified because the carbonate scale is thicker than the maximum depth analysed by XPS. The loss of the Mn signal could even attest of the scale high density.

The SEM/XPS coupled study highlighted lot of surface evolutions during the corrosion process under several temperatures and immersion time conditions. Once immersed in the brine heated to 50 °C, the carbon steel starts on oxidizing from the first hour of exposure and calcite scales appear after 2 days under same constant temperature conditions. The corrosion product evolves to a two-phase calcite/siderite crust for 3 weeks immersion. When increasing brine temperature up to 100 °C, the two-phase carbonates scale sets up from the first hours of exposure and keep on thickening with immersion time. SEM images have shown that the crystallites were growing up with time of exposure and this phenomenon enhances at higher temperature.

The research work by Esmaeely et al. has shown the impact of Ca^{2+} on the carbon steel CO_2 corrosion, with the appearance of $CaCO_3$ onto the material surface (Esmaeely et al., 2017). Nevertheless, the experiments were made at low CO_2 partial pressure. Zhao et al. expected that a high CO_2 partial pressure would result in a mixture of $FeCO_3$ and $CaCO_3$ (Zhao et al., 2005). This assumption is checked in this paper. Indeed, $CaCO_3$ solubility is approximately two orders of magnitude greater than $FeCO_3$ solubility (Mansoori et al., 2019). Indeed, at 25 °C and atmospheric pressure the solubility product constant K_{sp} of siderite in water is $K_{sp}(FeCO_3)= 1.28.10^{-11}$ (Wei, 2006) whereas for calcite, the value is $K_{sp}(CaCO_3) = 3.3.10^{-9}$ (Plummer and Busenberg, 1982). However, initially only calcium ions were present in the brine and afterwards Fe^{2+} ions appeared into the medium because of the metal dissociation during the corrosion process. Moreover, the quantity of CO_2 dissolved is more important at 50 °C as determines in our previous work (Poulain et al., 2019), with the study of the carbon dioxide solubility in Na-Ca-Cl aqueous solution saturated with CO_2 at 50 °C and 100 °C. Actually, the CO_2 solubility decreases when the temperature increases: from 0.257 mol kg^{-1} of water at 50 °C to 0.142 mol kg^{-1} of water at 100 °C. Therefore, in a first time, one can consider the

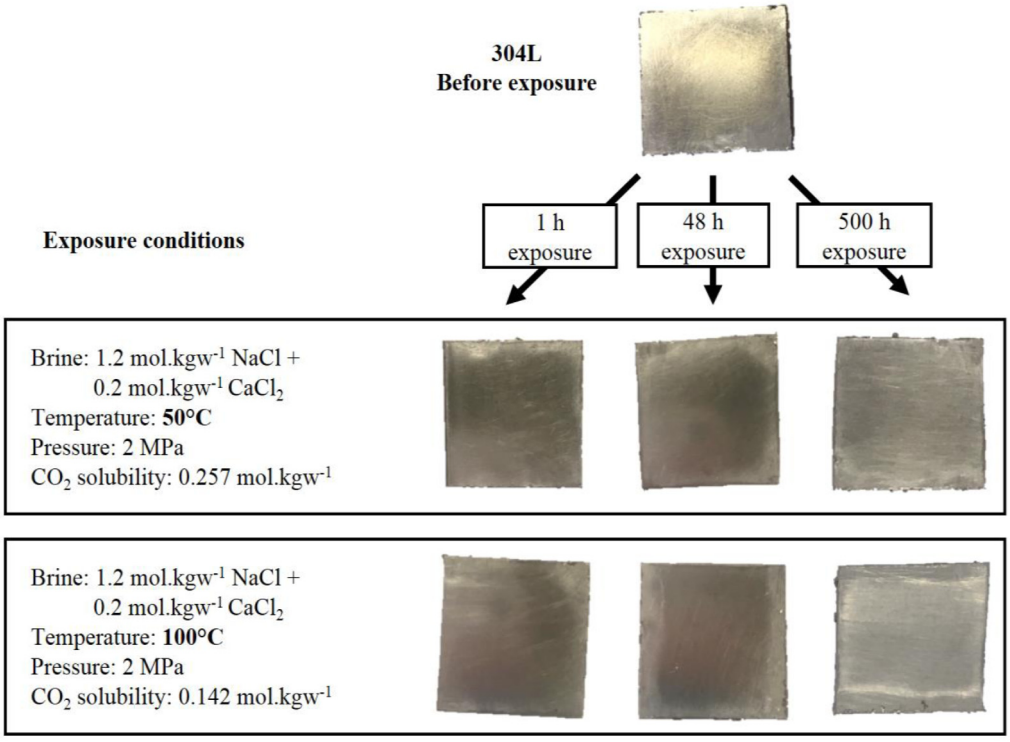

Fig. 10. Photographs of the stainless steel 304L specimens before and after their immersion into the geothermal fluid saturated with 2 MPa of CO_2 at 50 and 100 °C during 1, 48 and 500 h.

$CaCO_3$ precipitation is the favoured event onto the metal substrate. Furthermore, both $CaCO_3$ and $FeCO_3$ solubilities decrease when the brine temperature goes up and the precipitation of these two phases is then accelerated. This is the main reason that explains the scale consisting of a mixture of $CaCO_3$ and $FeCO_3$ is detected from the first hour of exposure at 100 °C. Finally, such corrosion products are generally porous but they become more compact when the temperature increases (Dugstad, 1998). SEM images highlight the corrosion layer densification at 100 °C acting as a passive barrier against corrosion continuation.

3.2. Stainless steel

To offer a point of comparison in relation with composition ans structure discrepancy, 304L stainless steel was studied under same conditions of brine corrosion.

Some photographs, before and after immersion into the CO_2-saturated brine at 50 °C and 100 °C during several exposure times, are displayed on Fig. 10. At first sight, no visible surface modification is noticed. Indeed, the surface still shiny appearance still exist whatever the treatment and the polishing scratches are still pronounced on the top surface.

To enhance perception of surface details, some optical microscopic images presented in Fig. 11 confirm the first naked eye observations. Nevertheless, the absence of changes of specimen visual aspect does not certify the absence of chemical modification. Chemical investigations engaged with XPS have provided additional information and have shown chemical evolutions.

Figs. 12 and 13 show core ionization peaks for O 1s and Cr $2p_{3/2}$ for stainless steel specimen before and after brine exposure. The quantitative analysis and the binding energies are reported in Table 3.

Analysis of the O 1s spectrum highlighted strong surface modifications before and after the treatment. Before exposure (Fig. 12a), four components can be distinguished reflecting several chemical environments given in Table 3 (Biesinger et al., 2011). The component

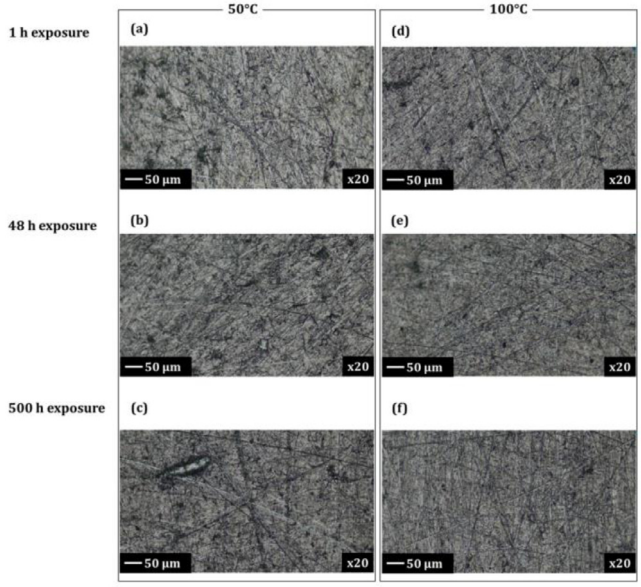

Fig. 11. Optical microscopic images of the stainless steel 304L specimens after immersion into the geothermal fluid saturated with 2 MPa of CO_2 at 50 °C during 1 h (a); 48 h (b); 500 hours (c) and at 100 °C during 1 h (d); 48 h (e) and 500 h (f).

located at 530.1 eV is characteristic of metal oxides when a metal hydroxides component is found at 531.2 eV. Concerning O–C=O and C–O components, they are respectively detected at 531.7 and 533 eV.

When 304L stainless steel is immersed into the brine heated up to 50 °C, a clear decrease of the metal oxide proportion on the sample surface is quickly observed (from 20.2 at.% before exposure to 10.7 at.% after 1 h exposure and down to 9.3 at.% after 500 h (Fig. 12a,b,d)). Otherwise, a significant enhancement of the metal hydroxide component

Table 3
Binding energies (BE) and atomic percentages (at.%) of the chemical environment identified by XPS on the stainless steel 304L surface before and after exposure to the geothermal fluid at 50 and 100 °C during several exposure times.

	Before exposure			50 °C					100 °C				
						1 h exposure	48 h exposure	500 h exposure			1 h exposure	48 h exposure	500 h exposure
Orbital	BE (eV)	Assignment	at.%	BE (eV)	Assignment	at.%	at.%	at.%	BE (eV)	Assignment	at.%	at.%	at.%
C 1s	282.9	Carbide	2.5	282.9	Carbide	1.8	2.6	2.4	282.9	Carbide	2.4	2.3	5.0
	285	C–C/C–H	28.4	285	C–C/C–H	29.8	15.4	17.5	285	C–C/C–H	22.7	23.1	17.4
	286.5	C–O	6.2	286.5	C–O	6.0	4.5	4.6	286.5	C–O	5.0	5.2	3.5
	288.5	O–C=O	3.7	288.5	O–C=O	2.0	1.3	1.2	288.5	O–C=O	1.7	1.2	0.9
				289.9	CO_3^{2-}	2.0	3.2	3.1	289.9	CO_3^{2-}	2.1	2	1.2
Ca 2p	347.5	$CaCO_3$	0.06	347.5	$CaCO_3$	0.1	0.5	0.4	347.5	$CaCO_3$	0.4	0.5	0.3
	351	$CaCO_3$	0.03	351	$CaCO_3$	0.05	0.3	0.2	351	$CaCO_3$	0.2	0.2	0.1
Cl 2p	198.8	Cl	0.2	198.8	Cl	0.7	1.7	0.2	198.8	Cl	0.4	0.5	0.3
	200.2	Cl	0.1	200.2	Cl	0.3	0.9	0.1	200.2	Cl	0.2	0.2	0.1
Fe 2p3/2	707	Fe^0	1.9	707	Fe^0	1.0	1.4	1.0	707	Fe^0	1.4	1.0	2.0
	709	Fe^{2+}	1.2	710.3	$FeCO_3$	1.0	1.0	0.7	710.3	$FeCO_3$	0.9	0.5	0.1
	710.8	Fe^{3+}	4.5	711.2	Fe^{3+}	1.3	0.2	0.3	711.2	Fe^{3+}	0.3	0.3	0.4
	714.7	Fe^{2+} sat.	0.2	715.0	$FeCO_3$ sat.	0.1	0.1	0.1	715.0	$FeCO_3$ sat.	0.1	0.1	
	718.8	Fe^{3+} sat.	0.1	719.2	Fe^{3+} sat.	0.1	0.1	0.1	719.2	Fe^{3+} sat.	0.1	0.1	0.1
Cr 2p3/2	574.4	Cr^0	1.0	574.4	Cr^0	0.9	1.4	1.2	574.4	Cr^0	1.2	0.9	1.4
	576	Cr_2O_3	0.6	576	Cr_2O_3	0.8	0.7	0.7	576	Cr_2O_3	1.2	0.6	0.8
	577	Cr_2O_3	0.6	577	Cr_2O_3	0.8	0.7	0.7	577	Cr_2O_3	1.2	0.6	0.8
	577.5	$Cr(OH)_3$	0.4	577.5	$Cr(OH)_3$	2.5	6.5	6.8	577.5	$Cr(OH)_3$	3.5	6.1	6.7
	577.8	Cr_2O_3	0.3	577.8	Cr_2O_3	0.4	0.3	0.4	577.8	Cr_2O_3	0.6	0.3	0.4
Ni 2p3/2	853	Ni^0	0.7	853	Ni^0	0.5	0.6	0.4	853	Ni^0	0.6	0.4	1.3
N 1s	400	NH_3	0.9	400	NH_3	0.8	0.5	0.6	400	NH_3	0.7	1.0	0.5
Na 1s				1072	NaCl		1.6	0.1	1072	NaCl	0.1	0.2	
O 1s	530.1	Oxide	20.2	530.2	Oxide	10.7	9.6	9.3	530.2	Oxide	7.2	5.0	7.5
	531.2	Hydroxide	6.8	531.2	Hydroxide	9.3	18.8	24.0	531.2	Hydroxide	19.7	20.0	28.3
	531.7	O–C=O	9.1	531.7	O–C=O	8.0	4.7	3.5	531.7	O–C=O	4.6	6.3	2.0
	533	C–O	6.4	532.1	CO_3^{2-}	7.9	10.4	10.0	532.1	CO_3^{2-}	10.9	9.3	5.4
				533.1	C–O	8.2	6.8	6.4	533.1	C–O	7.3	7.4	4.3
Si 2p	100.5	Si–C	2.6	100.5	Si–C	1.8	2.8	2.6	100.5	Si–C	2.3	2.8	5.9
	102	Si–CO, SiOx...	1.3	102	Si–CO, SiOx...	1.2	1.4	1.4	102	Si–CO, SiOx...	1.0	1.9	3.3

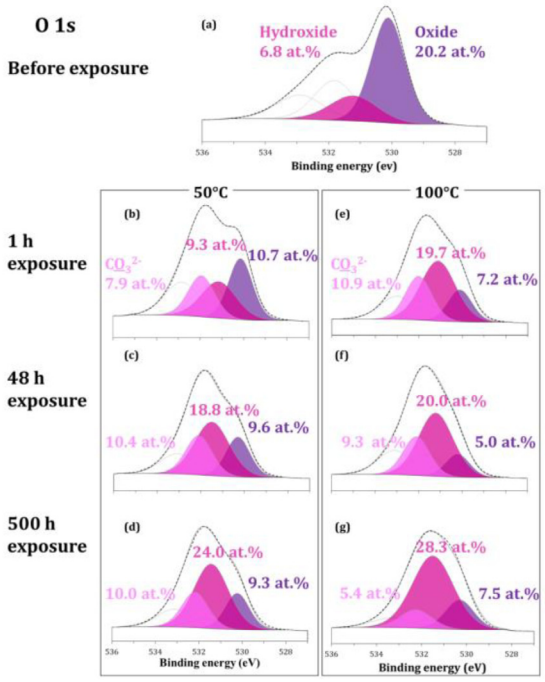

Fig. 12. O 1s XPS spectra of the stainless steel 304L specimens before immersion (a) and after immersion into the geothermal fluid saturated with 2 MPa of CO_2 at 50 °C during 1 h (b); 48 h (c); 500 h (d) and at 100 °C during 1 h (e); 48 h (f) and 500 h (g).

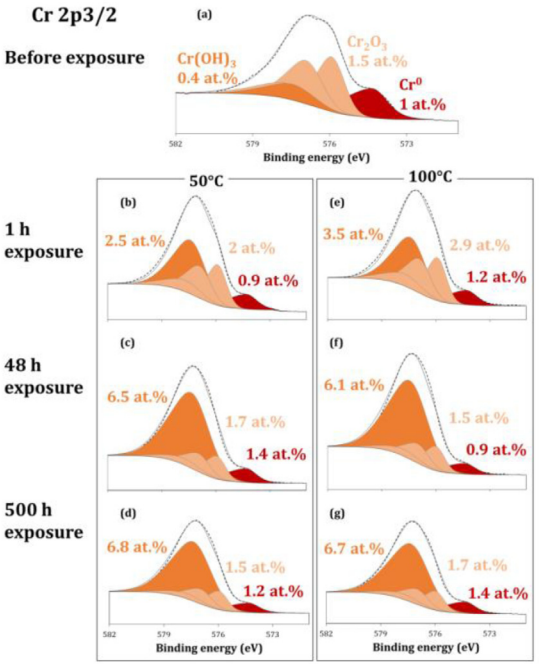

Fig. 13. Cr 2p3/2 XPS spectra of the stainless steel 304L specimens before immersion (a) and after immersion into the geothermal fluid saturated with 2 MPa of CO_2 at 50 °C during 1 h (b); 48 h (c); 500 h (d) and at 100 °C during 1 h (e); 48 h (f) and 500 h (g).

(from 6.8 at.% for raw material to 24.0 at.% after 500 h in the corrosion conditions) is remarkable. Biesinger et al. (2011), Maurice et al. (1994) Finally, the appearance of the carbonates peak at 532 eV (Fig. 12b) is noticed from the very first hour of the coupon immersion (Heuer and Stubbins, 1999; Cui et al., 2006; Wu et al., 2004). The proportion of this last component increases with the exposure time, as shown in Fig. 12b, c, d.

Concerning the specific treatment at 100 °C, XPS analyses globally show a same trend than 50 °C: a decrease of the metal oxide layer or phase, an increase of the metal hydroxide content and the

appearance of a carbonates component for a short time exposure (<500 h) (Fig. 12 g). Actually, under 100 °C conditions, the carbonate proportion has decreased whereas the metal oxide proportion has increased.

For the chromium survey, before the metal immersion into the brine, the Cr $2p_{3/2}$ core peak exhibits five components corresponding to three different environments (Table 3) : a chromium metal Cr^0 component at 574.4 eV and three components traducing a Cr_2O_3 environment respectively at 576.0, 577.0 and 577.8 eV and finally, a component assigned to chromium hydroxide at 577.5 eV (Biesinger et al., 2011; Lothongkum et al., 2003; Kocijan et al., 2007).

Whatever the temperature of the brine, the analysis of chromium XPS spectrum reveals some very similar results. Cr^0 and Cr_2O_3 components are still visible on the stainless steel surface in a relatively stable proportion, respectively around 1 at.% and 2 at.%. Furthermore, a clear increase of the $Cr(OH)_3$ content is noticed, in accordance with the increase of metal hydroxide component observed for the O 1s spectra. Biesinger et al. (2011), Maurice et al. (1994) These observations suggest the formation of a scale of chromium hydroxide from the first hours of exposure, according to the following equations (Guo et al., 2012; Xu et al., 2013; Liu et al., 2016; Chen et al., 2005, 2011):

$$Cr \rightarrow Cr^{3+} + 3e^- \quad (1)$$

$$Cr^{3+} + 3H_2O \rightarrow Cr(OH)_3 + 3H^+ \quad (2)$$

As done for chromium, the nickel, one of the main alloying element of 304L stainless steel (Table 1), was studied in terms of content and chemical environment. A first peak detected at 853.0 eV has informed the presence of Ni^0 at the surface, as reported in Table 3 (Biesinger et al., 2011). No particular evolution of this peak was recorded during the corrosion test and whatever the temperature and time conditions. The standard electrode potential of nickel ($Ni^{2+}/Ni°$ ($E° = -0{,}25V/SHE$ at 25 °C) could explain the relative protection of this metal compared to iron ($Fe^{2+}/Fe°$ ($E° = -0{,}44V/SHE$ at 25 °C)) or chromium ($Cr^{2+}/Cr°$ ($E° = -0{,}9V/SHE$ at 25 °C), $Cr^{3+}/Cr°$ ($E° = -0{,}74V/SHE$ at 25 °C)) for example. The element location in the sub-surface could even be a sufficient reason.

Iron metal in the 304L stainless steel composition is quite complex. Core ionization spectrum Fe $2p_{3/2}$(not shown in this paper) is composed of 5 components before exposure (Table 3): at 707.0 eV, a well-defined component corresponds to the iron metal Fe^0 when some the Fe^{2+} and Fe^{3+} oxidation states components are respectively found at 709.1 and 711.0 eV with their associated satellites peaks at 714.7 and 719.0 eV.

Into the geothermal fluid at 50 °C, some significant changes are noticed on the Fe $2p_{3/2}$ spectrum of the 304L stainless steel clearly evolved (Table 3). Even if the iron metal is still detected at 707.0 eV, the component content is at least as low as half (after 1 h immersion), probably indicating the beginning of the corrosion process with the metal oxidation process. For longer exposure time, this proportion remains quite stable. In a same time, the main and satellites component of Fe^{2+} oxidation state are no longer identified and Fe^{3+} components are still defined in reduced proportion (15 times less important after 500 h of exposure, Table 3). It could be explained by the growth of a corrosion product scale on the surface, which lowers the signal perception. Nevertheless, the iron and nickel metal components are still visible onto the near surface. Finally, the appearance of a peak at 710.3 eV and its associated satellite at 715.0 eV indicates the presence of iron carbonates on the 304L stainless steel surface from the first hour immersion. However, iron carbonates proportion is relatively stable (around 1.0 at.%, Table 3) whatever the time of exposure.

When the 304L stainless steel is immersed into the brine at 100 °C, the Fe $2p_{3/2}$ spectra reveal few changes compared to 50 °C. Iron metal is still observed on the contrary to Fe^{2+} state; on the other hand the proportion of the Fe^{3+} diminishes from 1 h exposure to 48 h exposure, probably reflecting the attack of the iron oxide passivation layer. Furthermore, the appearance of an iron carbonates scale from the first hour of corrosion test is remarkable. Nevertheless, there is a slight increase of the Fe^{3+} proportion on 304L stainless steel surface during 500 h and a simultaneous decrease of iron carbonates proportion is recorded. These observations are in accordance with the O 1s oxide component and O 1s carbonate component decrease at 100 °C during 500 h. These particular modifications remind those observed previously for the DC01 carbon steel surface under the same operating conditions. A likely partial oxidation of the siderite scale would occur when sample is dried to air after the treatment, as previously shown by Heuer and Stubbins (Heuer and Stubbins, 1999).

Globally, results obtained for the immersed 304L stainless steel at 50 °C and 100 °C do not exhibit remarkable differences. The presence of chromium in the metal composition, with the inherent formation of a chromium oxide scale on the surface, an even the nickel existence, participate, as an evidence, in the protection of the material against the surface corrosion. The chemical nature of the corrosion products on the stainless steel surface is different from carbon steel. It consists in a mixture of $FeCO_3$ and $Cr(OH)_3$. These corrosion products were previously identified in the work of Yue which was conducted at 200 °C and 2.85 MPa (Yue, 2020). As a matter of fact, carbon seems to be a minor resource in the passive barrier effect from a chemical composition and microstructure points of view (Iberl et al., 2015). We can also notice that no pitting has occurred on the stainless steel surfaces in these experimental conditions. However, further electrochemical investigations would help to characterize pitting corrosion. Mundhenk et al. have demonstrated the stainless steel 316L, which contains more molybdenum than the 304 L, did not exhibit any visible attack but potentiodynamic polarization measurements showed a tendency to favour pitting corrosion in experimental conditions close to this study (Mundhenk et al., 2013a).

4. Conclusion

In this paper, a laboratory pilot has been designed specifically for material corrosion testing in complex environment. By the use of this prototype, the geothermal corrosion behaviours of two materials, a carbon steel DC01 and a stainless steel 304L, were investigated under specific conditions of fluid composition, temperature and time exposure. The simulated fluid consisted in a brine composed of NaCl and $CaCl_2$ saturated with 2 MPa of carbon dioxide. Corrosion tests were conducted at 50 °C and 100 °C. After the corrosion tests, surface samples characterizations were achieved and shown that the nature of the corrosion products was quite different in regard to the substrate composition. Some calcite $CaCO_3$ phases co-existing with siderite $FeCO_3$ grew up on the carbon steel surface whereas siderite $FeCO_3$ and chromium hydroxide $Cr(OH)_3$ spread over the stainless steel. The nature of corrosion product, in particular the XPS identification of $CaCO_3$, confirms the important role of the water chemistry through the presence of calcium ions. Moreover, the impact of the temperature and therefore the CO_2 dissolved concentration should postulate the corrosion products formed faster at high temperature in the case of carbon steel. The resulting scale seemed to be denser and more protective, representing a barrier against uniform corrosion. Stainless steel corrosion study did not clearly show any impact of the brine temperature. Indeed, a scale of $Cr(OH)_3$ and $FeCO_3$ is formed whatever the experimental conditions and appears as dense surface barrier.

In this work, the geothermal-like corrosion study at high temperature confirmed that the stainless steel was more corrosion resistant than the carbon steel. Consequently, the 304L stainless steel constitute a more appropriate material to be used in geothermal equipment with these brine conditions. The use of surface methods such as XPS and SEM allows to conduct a complete and genuine characterization of the material corroded surface. Moreover, the study of several times of exposure gives a better comprehension of the corrosion mechanism process. Further investigations on the microstructure impact would contribute to improve this understanding.

Declaration of competing interest

The authors declare that they have no known competing financial interests or personal relationships that could have appeared to influence the work reported in this paper.

Acknowledgement

This work was supported by GIS GEODENERGIES (Carphymcheau), France and Institut Carnot ISIFoR, France.

References

Agemar, T., Weber, J., Schulz, R., 2014. Deep geothermal energy production in Germany. Energies 7, 4397–4416. http://dx.doi.org/10.3390/en7074397.

ASTM G1-03, 2018. Standard Practice for Preparing, Cleaning, and Evaluating Corrosion Test Specimens. ASTM International, West Conshohocken, PA, URL: https://www.astm.org/g0001-03r17e01.html.

Biesinger, M.C., Payne, B.P., Grosvenor, A.P., Lau, L.W.M., Gerson, A.R., Smart, R.St.C., 2011. Resolving surface chemical states in XPS analysis of first row transition metals, oxides and hydroxides: Cr, Mn, Fe, Co and Ni. Appl. Surf. Sci. 257, 2717–2730. http://dx.doi.org/10.1016/j.apsusc.2010.10.051.

Carter, J.P., Cramer, S.D., 1992. Materials of Construction for High-Salinity Geothermal Brines. US Bureau of Mines, Spokane, WA.

Chen, C.F., Lu, M.X., Sun, D.B., Zhang, Z.H., Chang, W., 2005. Effect of chromium on the pitting resistance of oil tube steel in a carbon dioxide corrosion system. Corrosion 61.

Chen, T., Xu, L., Lu, M., Chang, W., Zhang, L., 2011. Study on factors affecting low Cr alloy steels in a CO_2 corrosion system.

Corsi, R., 1986. Scaling and corrosion in geothermal equipment: problems and preventive measures. Geothermics 15, 839–856. http://dx.doi.org/10.1016/0375-6505(86)90097-0.

Cui, Z.D., Wu, S.L., Zhu, S.L., Yang, X.J., 2006. Study on corrosion properties of pipelines in simulated produced water saturated with supercritical CO_2. Appl. Surf. Sci. 252, 2368–2374. http://dx.doi.org/10.1016/j.apsusc.2005.04.008.

Culivicchi, G., Palmerini, C.G., Scolari, V., 1983. Behaviour of materials in geothermal environments. Geothermics 14, 73–90. http://dx.doi.org/10.1016/0375-6505(85)90095-1.

Dugstad, A., 1998. Mechanism of protective film formation during CO_2 corrosion of carbon steel. In: NACE International (Ed.) CORROSION 98.

Esmaeely, S.N., Young, D., Brown, B., Nešić, S., 2017. Effect of incorporation of calcium into iron carbonate protective layers in CO_2 corrosion of mild steel. Corrosion 73, 238–246. http://dx.doi.org/10.5006/2261.

Faes, W., Lecompte, S., Van Bael, J., Salenbien, R., Bäßler, R., Bellemans, I., Cools, P., De Geyter, N., Morent, R., Verbeken, K., De Paepe, M., 2019. Corrosion behaviour of different steel types in artificial geothermal fluids. Geothermics 82, 182–189. http://dx.doi.org/10.1016/j.geothermics.2019.05.018.

Frick, S., Regenspurg, S., Kranz, S., Milsch, H., Saadat, A., Francke, H., Brandt, W., Huenges, E., 2011. Geochemical and process engineering challenges for geothermal power generation. Chem. Ing. Tech. 83, 2093–2104. http://dx.doi.org/10.1002/cite.201100131.

Guo, S., Xu, L., Zhang, L., Chang, W., Lu, M., 2012. Corrosion of alloy steels containing 2% chromium in CO_2 environments. Corros. Sci. 63, 246–258. http://dx.doi.org/10.1016/j.corsci.2012.06.006.

Guo, S., Xu, L., Zhang, L., Chang, W., Lu, M., 2016. Characterization of corrosion scale formed on 3Cr steel in CO_2-saturated formation water. Corros. Sci. 110, 123–133. http://dx.doi.org/10.1016/j.corsci.2016.04.033.

Heuer, J.K., Stubbins, J.F., 1999. An XPS characterization of $FeCO_3$ films from CO_2 corrosion. Corros. Sci. 41, 1231–1243. http://dx.doi.org/10.1016/S0010-938X(98)00180-2.

Huttenloch, P., Zorn, R., Makni, L., Steger, H., Schilling, F., Hater, W., 2019. Inhibitor performance on carbon steel in the geothermal environment of the Upper Rhine graben (Central Europe)–A laboratory study. Geothermics 81, 198–208. http://dx.doi.org/10.1016/j.geothermics.2019.05.007.

Iberl, P., Alt, N.S.A., Schluecker, E., 2015. Evaluation of corrosion of materials for application in geothermal systems in Central Europe: Evaluation of corrosion of materials in geothermal systems. Mater. Corros. 66, 733–755. http://dx.doi.org/10.1002/maco.201407864.

Kaya, T., Hoshan, P., 2005. Corrosion and material selection for geothermal systems. In: Proceedings World Geothermal Congress, World Geothermal Congress. Anatalya (Turkey).

Keserović, A., 2014. Geothermal Systems in Indonesia - Influence on the Corrosion Resistance of Stainless Steel Materials. Technische Universität Berlin.

Klapper, H.S., Baessler, R., Weidauer, K., Stuerzbecher, D., 2012. Evaluation of suitability of high-alloyed materials for geothermal applications in the North German Basin. Corrosion 68, 016001-1-016001–9. http://dx.doi.org/10.5006/1.3676631.

Kocijan, A., Donik, Č., Jenko, M., 2007. Electrochemical and XPS studies of the passive film formed on stainless steels in borate buffer and chloride solutions. Corros. Sci. 49, 2083–2098. http://dx.doi.org/10.1016/j.corsci.2006.11.001.

Liu, Z., Gao, X., Li, J., Du, L., Yu, C., Li, P., Bai, X., 2016. Corrosion behaviour of low-alloy martensite steel exposed to vapour-saturated CO_2 and CO_2-saturated brine conditions. Electrochim. Acta 213, 842–855. http://dx.doi.org/10.1016/j.electacta.2016.08.024.

Lopez, D.A., Schreiner, W.H., de Sanchez, S.R., Simison, S.N., 2003. The influence of carbon steel microstructure on corrosion layers an XPS and SEM characterization. Appl. Surf. Sci. 69–85. http://dx.doi.org/10.1016/S0169-4332(02)01218-7.

Lothongkum, G., Chaikittisilp, S., Lothongkum, A.W., 2003. XPS investigation of surface films on high Cr-Ni ferritic and austenitic stainless steels. Appl. Surf. Sci. 218, 203–210. http://dx.doi.org/10.1016/S0169-4332(03)00600-7.

Mansoori, H., Brown, B., Young, D., Nesic, S., Singer, M., 2019. Effect of calcium ions and $CaCO_3$ scale on the CO_2 corrosion mechanism of mild steel.

Maurice, V., Yang, W.P., Marcus, P., 1994. XPS and STM investigation of the passive film formed on Cr(110) single-crystal surfaces. J. Electrochem. Soc. 141, 3016–3027. http://dx.doi.org/10.1149/1.2059274.

Mouchot, J., Genter, A., Cuenot, N., Scheiber, J., Seibel, O., Bosia, C., Ravier, G., 2018. First year of operation from EGS geothermal plants in Alsace, France: Scaling issues. Stanford, California.

Mundhenk, N., Carrero, S., Knauss, K.G., Wonneberger, R., Undisz, A., Wu, Y., 2020. Kinetic and thermodynamic analysis of high-temperature CO_2 corrosion of carbon steel in simulated geothermal NaCl fluids. Corros. Sci. 108597. http://dx.doi.org/10.1016/j.corsci.2020.108597.

Mundhenk, N., Huttenloch, P., Bäßler, R., Kohl, T., Steger, H., Zorn, R., 2014. Electrochemical study of the corrosion of different alloys exposed to deaerated 80 °C geothermal brines containing CO_2. Corros. Sci. 84, 180–188. http://dx.doi.org/10.1016/j.corsci.2014.03.027.

Mundhenk, N., Huttenloch, P., Kohl, T., Steger, H., Zorn, R., 2013a. Metal corrosion in geothermal brine environments of the upper Rhine graben – Laboratory and on-site studies. Geothermics 46, 14–21. http://dx.doi.org/10.1016/j.geothermics.2012.10.006.

Mundhenk, N., Huttenloch, P., Sanjuan, B., Kohl, T., Steger, H., Zorn, R., 2013b. Corrosion and scaling as interrelated phenomena in an operating geothermal power plant. Corros. Sci. 70, 17–28. http://dx.doi.org/10.1016/j.corsci.2013.01.003.

Nazari, M.H., Allahkaram, S.R., Kermani, M.B., 2010. The effects of temperature and pH on the characteristics of corrosion product in CO_2 corrosion of grade X70 steel. Mater. Des. 5. http://dx.doi.org/10.1016/j.matdes.2010.01.038.

Nogara, J., Zarrouk, S.J., 2018a. Corrosion in geothermal environment: Part 1: Fluids and their impact. Renew. Sustain. Energy Rev. 82, 1333–1346. http://dx.doi.org/10.1016/j.rser.2017.06.098.

Nogara, J., Zarrouk, S.J., 2018b. Corrosion in geothermal environment Part 2: Metals and alloys. Renew. Sustain. Energy Rev. 82, 1347–1363. http://dx.doi.org/10.1016/j.rser.2017.06.091.

Palacios, C.A., Shadley, J.R., 1991. Characteristics of corrosion scales on steels in a CO_2-saturated NaCl brine. Corrosion 47, 122–127. http://dx.doi.org/10.5006/1.3585227.

Plummer, L.N., Busenberg, E., 1982. The solubilities of calcite, aragonite and vaterite in $CO_2 - H_2O$ solutions between 0 and 90 °C, and an evaluation of the aqueous model for the system $CaCO_3$-CO_2–H_2O. Geochim. Cosmochim. Acta 46, 1011–1040. http://dx.doi.org/10.1016/0016-7037(82)90056-4.

Poulain, M., Messabeb, H., Lach, A., Contamine, F., Cézac, P., Serin, J.-P., Dupin, J.-C., Martinez, H., 2019. Experimental measurements of carbon dioxide solubility in Na–Ca–K–Cl solutions at high temperatures and pressures up to 20 MPa. J. Chem. Eng. Data. 64, 2497–2503. http://dx.doi.org/10.1021/acs.jced.9b00023.

Prawoto, Y., Ibrahim, K.M., Nik, W.S.W., 2009. Effect of pH and chloride concentration on the corrosion of duplex stainless steel. Arab. J. Sci. Eng. 34, 115–127.

Sanjuan, B., Millot, R., Innocent, Ch, Dezayes, Ch, Scheiber, J., Brach, M., 2016. Major geochemical characteristics of geothermal brines from the upper rhine graben granitic basement with constraints on temperature and circulation. Chem. Geol. 428, 27–47. http://dx.doi.org/10.1016/j.chemgeo.2016.02.021.

Tavares, L.M., da Costa, E.M., de O. Andrade, J.J., Hubler, R., Huet, B., 2015. Effect of calcium carbonate on low carbon steel corrosion behavior in saline CO_2 high pressure environments. Appl. Surf. Sci. 359, 143–152. http://dx.doi.org/10.1016/j.apsusc.2015.10.075.

Wang, Y.-Y., Kusumoto, K., Li, C.-J., 2012. XPS analysis of SiC films prepared by radio frequency plasma sputtering. Phys. Procedia 32, 95–102. http://dx.doi.org/10.1016/j.phpro.2012.03.524.

Wei, S., 2006. Kinetics of Iron Carbonate and Iron Sulfide Scale Formation in CO_2/H_2S Corrosion. Faculty of the Russ College of Engineering and Technology of Ohio University.

Wu, S.L., Cui, Z.D., He, F., Bai, Z.Q., Zhu, S.L., Yang, X.J., 2004. Characterization of the surface film formed from carbon dioxide corrosion on N80 steel. Mater Lett. 58, 1076–1081. http://dx.doi.org/10.1016/j.matlet.2003.08.020.

Xu, L., Guo, S., Chang, W., Chen, T., Hu, L., Lu, M., 2013. Corrosion of Cr bearing low alloy pipeline steel in CO_2 environment at static and flowing conditions. Appl. Surf. Sci. 270, 395–404. http://dx.doi.org/10.1016/j.apsusc.2013.01.036.

Yevtushenko, O., Baessler, R., 2012. Electrochemical studies on pitting corrosion on Cr13 steel exposed to CO_2 and artificial brine with high chloride. In: Materials Challenges and Testing for Supply of Energy and Resources. Springer-Verlag Berlin Heidelberg, pp. 45–53.

Yevtushenko, O., Bäßler, R., Pfennig, A., 2010. Corrosion behaviour of Cr13 steel in CO_2 saturated brine with high chloride concentration: Corrosion behaviour of Cr13 steel in CO_2 saturated brine. Mater. Corros. 63, 517–521. http://dx.doi.org/10.1002/maco.201005932.

Yue, X., 2020. A thermodynamic and kinetic study of the formation and evolution of corrosion product scales on 13Cr stainless steel in a geothermal environment. Corros. Sci. 16. http://dx.doi.org/10.1016/j.corsci.2020.108640.

Zhao, G.-X., Li, J.-P., Hao, S.-M., Lü, X.-H., Li, H.-L., 2005. Effect of Ca^{2+} and Mg^{2+} on CO_2 corrosion behavior of tube steel. J. Iron Steel Res. Int. 12, 38–42.